ANNALS OF GEOPHYSICS, 66, 2, SE210, 2023; doi.10.4401/ag-8852
OPEN ACCESS

Seismic anisotropy in the upper crust around the north segment of Xiaojiang faults in the SE margin of Tibetan Plateau

Peng Wu[1,3,4], Yuan Gao[*,2], Lisheng Xu[1]

(1) Institute of Geophysics, China Earthquake Administration, Beijing 100081, China
(2) Key Laboratory of Earthquake Prediction, Institute of Earthquake Forecasting, China Earthquake Administration, Beijing 100036, China
(3) Hebei Hongshan National Observatory on Thick Sediments and Seismic Hazards, Xingtai 055350, China
(4) Handan Central Seismic Station, Hebei Earthquake Agency, Handan 056001, China

Article history: received May 30, 2022; accepted October 11, 2022

Abstract

The Xiaojiang faults located in the SE margin of the Tibetan Plateau is a fault system of left-lateral strike-slip, striking NS, between the 2nd-order Sichuan-Yunnan block and the 1st-order South China block. The Xiaojiang faults and the surrounding areas are characterized by strong tectonic movements and intense seismic activities. Using seismic data from January 2013 to November 2020 recorded at the stations of the temporary QiaoJia seismic Array (QJ Array), deployed by the Institute of Geophysics, China Earthquake Administration, this study investigates the upper crustal anisotropy by the shear-wave splitting analysis on small local earthquakes, discusses the deformation patterns in the upper crust in the north segment of the Xiaojiang faults, evaluates the stress distribution in the study area, and analyzes its relationship with the regional tectonic structure. Adopting the data processing technique of shear-wave splitting, a total of 875 effective records were obtained at 50 stations. The mean direction of polarizations of fast shear-wave (PFS) is 162° ± 44° in the study area and the mean normalized time-delay is 4.96 ± 2.38 ms/km. Based on the spatial distribution of the PFS and the regional geologic structure, the study area is divided into two zones: the zone N and the zone S. The PFS in the zone N is scattered, but the dominant PFS direction is in NNW, which is consistent with the direction of the regional maximum principal compressive stress. In the zone N, there are a few smaller local areas (i.e., subzones A, B, C, and D) in which the orientations of the PFS are quite different from the surrounding area. In the zone S, the dominant directions at most stations are in nearly NS, consistent with the strike of the Xiaojiang fault. It reveals the detailed spatial distribution of seismic anisotropy in the upper crust, as well as *in situ* principal compressive stress, indicating the influence of the regional stress, the complex tectonic environment, and maybe also the impact of the South China block. It also reveals that there also might be an upper-crust scale of tectonic line at near 26°20′N under Xiaojiang faults, which coincides with the north-south tectonic boundary in the lithospheric anisotropy.

Key words: Crustal seismic anisotropy; Xiaojiang fault; SE margin of the Tibetan Plateau; Shear-wave splitting; Crustal deformation

1. Introduction

Due to the collision between the Indian plate and the Eurasian plate, the Tibetan Plateau (TP) and its surrounding areas are characterized by strong tectonic movement and high seismicity, making it an ideal zone to investigate the continental collision and deep dynamic evolution in the Himalaya orogen in recent decades [Yin and Harrison, 2000; Sherrington et al, 2004; Zhang et al., 2011]. The southeastern (SE) margin of the TP is the tectonic transitional area between the South China block (SCB) and the TP, which is supposed to the significant zone for the TP material escape southeastward [Royden et al., 1997; Clark et al., 2000; Bai et al., 2010]. The crust in the southwestern margin of the Yangtze craton has been squeezed since the Cenozoic, forming several large-scale active faults, such as the Xiaojiang, Anninghe, and Zemuhe faults [Shen et al., 2005]. The clockwise rotation in the upper crust of the southeastern TP around the Eastern Himalayan Syntaxis results in a strong left-lateral shear movement in the Xianshuihe-Xiaojiang fault zone [Kreemer et al., 2014; Zheng et al., 2017].

Seismic anisotropy in the crust is ubiquitous [Crampin, 1978; Crampin et al., 1984, 2003, 2008; Gao et al., 1998, 2011; Savage, 1998; Gao and Crampin, 2006; Kaviris et al., 2015, 2018; Crampin and Gao, 2018; Cao et al., 2019; Jiang et al., 2021]. The characteristics of the crustal deformation, deep tectonic structure, and evolution mechanism of the geodynamics can be learned from the anisotropic information [Silver and Flesch, 2007; Kong et al., 2016; Yang et al., 2017; Huang et al., 2018; Zhang et al., 2018; Zheng et al., 2018; Jiang et al., 2021]. Shear-wave splitting (SWS) measurement is one of the effective ways to obtain the anisotropic parameters. Seismic shear-waves propagating through an anisotropic media are expected to split into two almost orthogonal components in different velocities: fast shear-waves and slow shear-waves [Crampin and Peacock, 2005; Long and Silver, 2008]. The polarization of the fast shear-wave (PFS) and the time delay of slow shear-wave (TDS) are two important SWS parameters. The PFS is generally consistent with the direction of the *in situ* principal compressive stress [Crampin et al., 2003; Gao et al., 1998, 2011], while the PFS at the stations located on active faults is parallel to the strike of the fault [Boness and Zoback, 2006; Gao et al., 2011]. The TDS is related to anisotropic degree of the medium [Gao and Crampin, 2004; Crampin and Peacock, 2005; Crampin et al., 2008; Gao et al., 2018].

The SWS parameters in the Yunnan province were obtained by local earthquake data from Yunnan regional seismograph network, showing the complicated orientations of the PFS in the upper crust, but obviously with a predominantly NS direction [Shi et al. 2012; Gao et al. 2012]. Tai et al. [2015] utilized the near-field seismic records from the ChinArray Phase I, a temporary seismic investigation project, to compute the crustal seismic anisotropy in the south of the North-South seismic belt. The dominant PFS is consistent with the direction of the regional principal compressive stress, but the PFS at some stations near faults is affected by the strike of the faults. Zhang and Gao [2017] analyzed the crustal anisotropy over the North-South seismic belt with data of the ChinArray Phase I plus Phase II. The results showed that the TDS in the south is higher than that in the north, suggesting a stronger tectonic deformation in the SE margin of the TP. With the seismic data of a local temporary seismic array, Liang et al. [2020] obtained preliminary anisotropic results in the north segment of the Xiaojiang fault zone (XJFZ), indicating the complicated spatial patterns of PFS in the study area. It is speculated that the fault strike plays a significant role in upper crustal anisotropy. Seismic anisotropy of teleseismic data have revealed that the upper mantle material from the SCB has possibly passed through the XJFZ westward to the west boundary of the Sichuan-Yunnan block (SYB) [Gao et al., 2020]. While the crustal anisotropy in the south segment of the XJFZ indicated that the influence on the SYB from of the SCB has expanded westwards to the interior of SYB in the upper crust [Li et al., 2021]. However, the previous studies are preliminary, limited by the number of seismic stations, observation locations and data quality. To better understand the relationships among the crustal deformation, faults characteristics and regional stress, this study uses the near-field seismic waveform data from a dense temporary seismic array around the north segment of XJFZ to obtain the crustal anisotropy in the study area and to analyze the detailed spatial characteristics in the upper crust and the crustal deformation implications.

2. Tectonic settings

Owing to the southeastward extrusion of material in the TP and the clockwise rotation of the SYB around the Eastern Himalayan Syntaxis [Liang et al., 2013], the XJF and its surrounding areas are characterized by intense tectonic movements and frequent seismic activities. The study area is situated between the SYB and the SCB, in which major active faults include Xiaojiang fault (XJF) and Puduhe fault (PDHF) striking NS, Ludian-Zhaotong fault (LZF)

and Lianfeng fault (LFF) striking NE (Figure 1). Several faults, such as the Zemuhe fault (ZMHF), Daliangshan fault (DLSF), and XJF, converge on the east of the Qiaojia County, exhibiting a complex tectonic structure. The XJF has a length of more than 400 km. It starts in the north of Qiaojia and stretches southward along the Jinsha River and the Xiaojiang Valley, terminating to the north of the Ailaoshan-Red River shear zone [Wang et al., 1998]. To the north of Dongchuan, the XJF is divided into two branches, i.e., the east XJF and the west XJF (Figure 1).

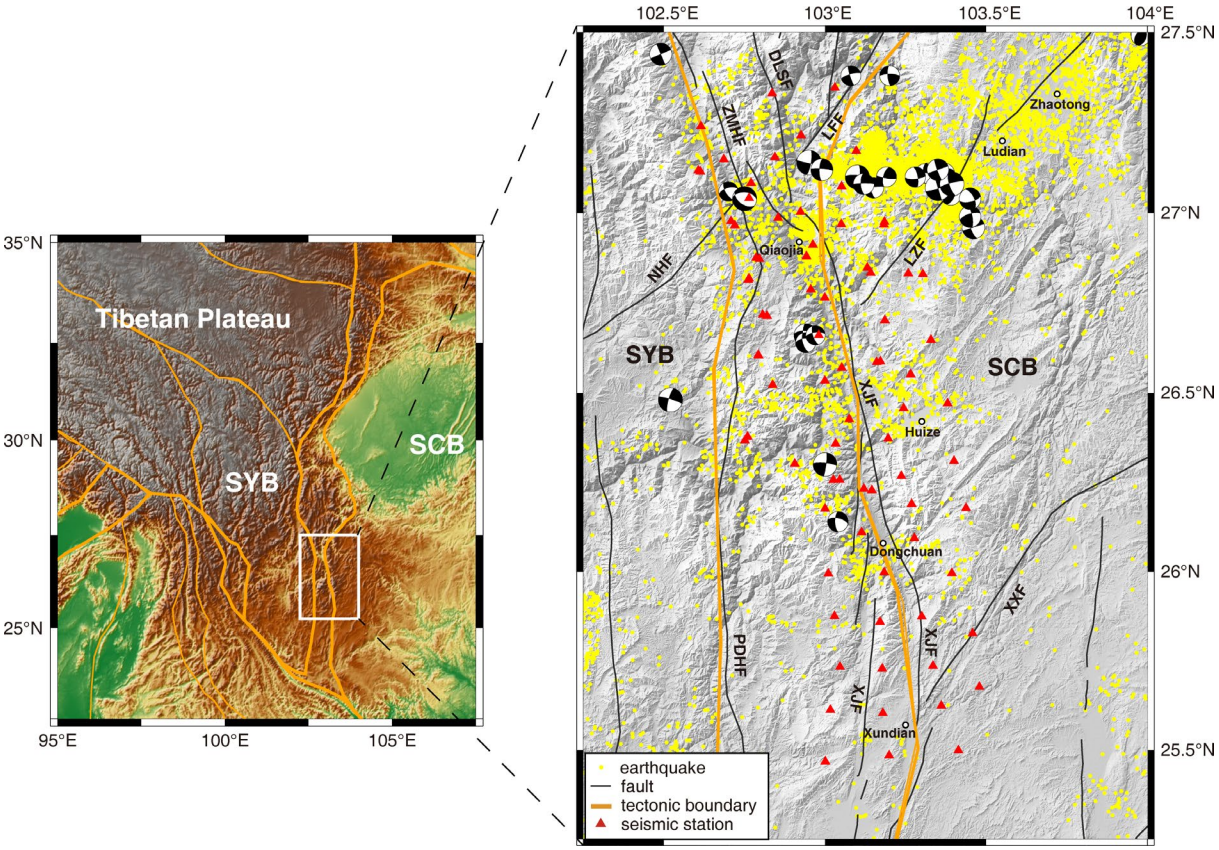

Figure 1. The seismotectonic map of the study area. The left is tectonic settings around the study area, and the white rectangle outlines the study area. The right is the distribution of faults, seismic stations, and hypocenters in the Xiaojiang fault system. Yellow dots represent the earthquakes with $M_L \leq 4.0$, recorded by the temporary Qiaojia Seismic Array from January 2013 to November 2020. Black beachballs depict the focal mechanisms of earthquakes with $M_L \geq 3.5$, occurring from January 2009 to May 2018 (Li et al, 2019). SCB: South China block; SYB: Sichuan-Yunnan block; XJF: Xiaojiang fault; PDHF: Puduhe fault; NHF: Ninghui fault; ZMHF: Zemuhe fault; DLSF: Daliangshan fault; LFF: Lianfeng fault; LZF: Ludian-Zhaotong fault; XXF: Xundian-Xuanwei fault.

Since 1500, four *M*7.0+ earthquakes have occurred in the XJFZ and its surrounding areas. Geological and geodetic surveys have shown that the annual slip rate is higher in the north of the XJF than that in the south [Xu et al., 2003; Shen et al., 2005]. Li et al. [2013] used the repeating microearthquakes to estimate that the slip rates at the depth of 3-12 km is 1.6-10.1 mm/a in the XJFZ, showing substantial differences in deep slip rates among different segments. The three-dimensional velocity model exhibited a low-velocity anomaly in the upper and middle crust beneath the XJFZ and high-velocity anomalies in its east [Wu et al., 2013; Zheng et al., 2016]. In the lower crust, it was hypothesized that a low-velocity anomaly in the middle of XJFZ is related to high temperature derived from the upper mantle, whereas a high-velocity anomaly in the north may be caused by a large amount of basic and ultrabasic mantle material intruding into the crust due to mantle plume activities in late Paleozoic. Zhao et al. [2020] presented a high-resolution three-dimensional crustal model of the SE margin of the TP obtained from a joint inversion of local earthquake P-wave travel-time and Bouguer gravity anomalies and believed that the crustal low-velocity zone beneath the XJFZ might have been caused by localized asthenosphere upwelling. The velocity profile derived

from active source wide-angle seismic data showed that the crustal velocity is lower in the XJFZ, indicating a lower rheological strength in the upper crust [Xu et al., 2014]. The focal mechanisms over the North-South seismic belt conducted by Wang et al. [2015] demonstrated that the orientation of the maximum horizontal compressive stress shows a clockwise rotational trend from north to south in the XJFZ, i.e., NW-NNW-NS direction. In addition, the magnetotelluric images displayed that the upper crust in the XJF and its surrounding areas is generally of high resistivity, probably revealing the crystalline basement rocks of the Yangtze craton [Li et al., 2019].

3. Data and methods

3.1 Data

The seismic data used in this study were obtained from the temporary QiaoJia Seismic Array (QJ Array), which was deployed in March 2012 by the Geophysical Institute of Geophysics, China Earthquake Administration. The QJ Array is composed of 81 temporary seismic stations in the northern segment of the XJFZ, with a station interval of 20 km. It is equipped with two observation systems: (1) Guralp CMG-3ESPCDE seismometers with a built-in 24-bit digitizer and a frequency bandwidth of 0.017 to 100 Hz. (2) Guralp CMG-40T seismometers with Reftek 130S digitizer and a frequency bandwidth of 0.03 to 100 Hz. The sampling rates of the two observation systems are 100 Hz. Finally, we collected 12827 local earthquake events with $M_L \leq 4.0$ (Figure 1), recorded by QJ Array from January 2013 to November 2020, to investigate the upper crustal anisotropy. The focal depth of local earthquakes was less than 25 km.

3.2 Methods

The SWS measurements were analyzed using the systematic analysis method (SAM) developed by Gao et al. [2004]. This method includes three aspects: the calculation of correlation function, the elimination of time delay, and the verification of polarization analysis. Total reflection occurs when the incident angle of a shear-wave propagating to the free surface is greater than the critical angle that is the limit range of the shear-wave window. The critical angle of the Poisson medium is about 35°, and the shear-wave window can be extended to 40-45°, considering the impact of the curved wavefront and low-velocity sedimentary layers on the crust surface [Crampin and Peacock,

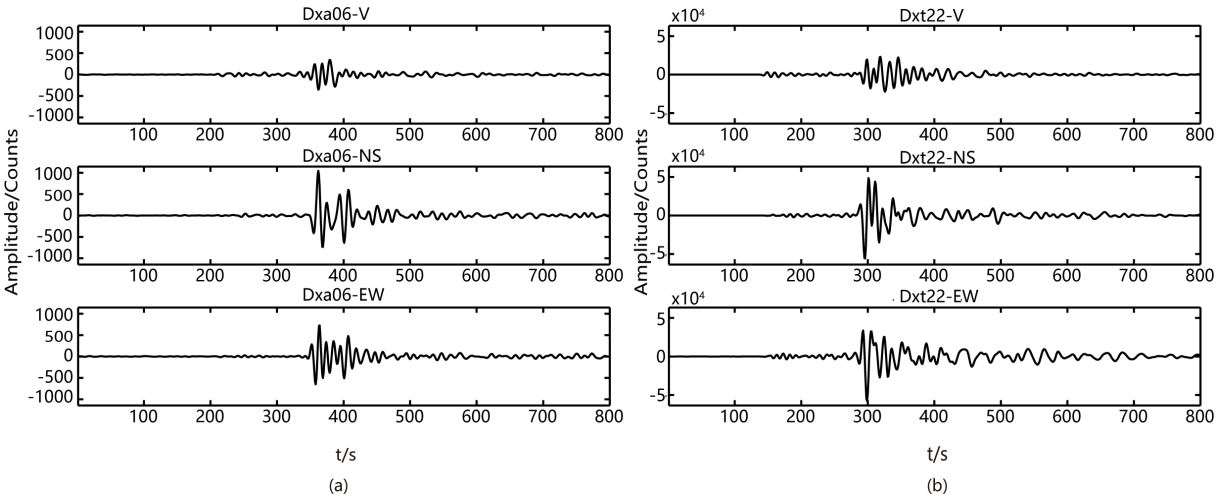

Figure 2. Seismic waveforms at two seismic stations. From top to bottom, the diagrams show vertical (V), north-south (NS), and east-west (EW) components, respectively. (a) The event recorded at Dxa06 occurred at UTC 18:37:48 on 7 December 2016, magnitude M_L 0.8, hypocentral depth 9 km, and epicentral distance 3.38 km; (b) The event recorded at Dxt22 occurred at UTC 08:26:36 on 1 June 2020, magnitude M_L 1.3, hypocentral depth 6 km, and epicentral distance 3.1 km.

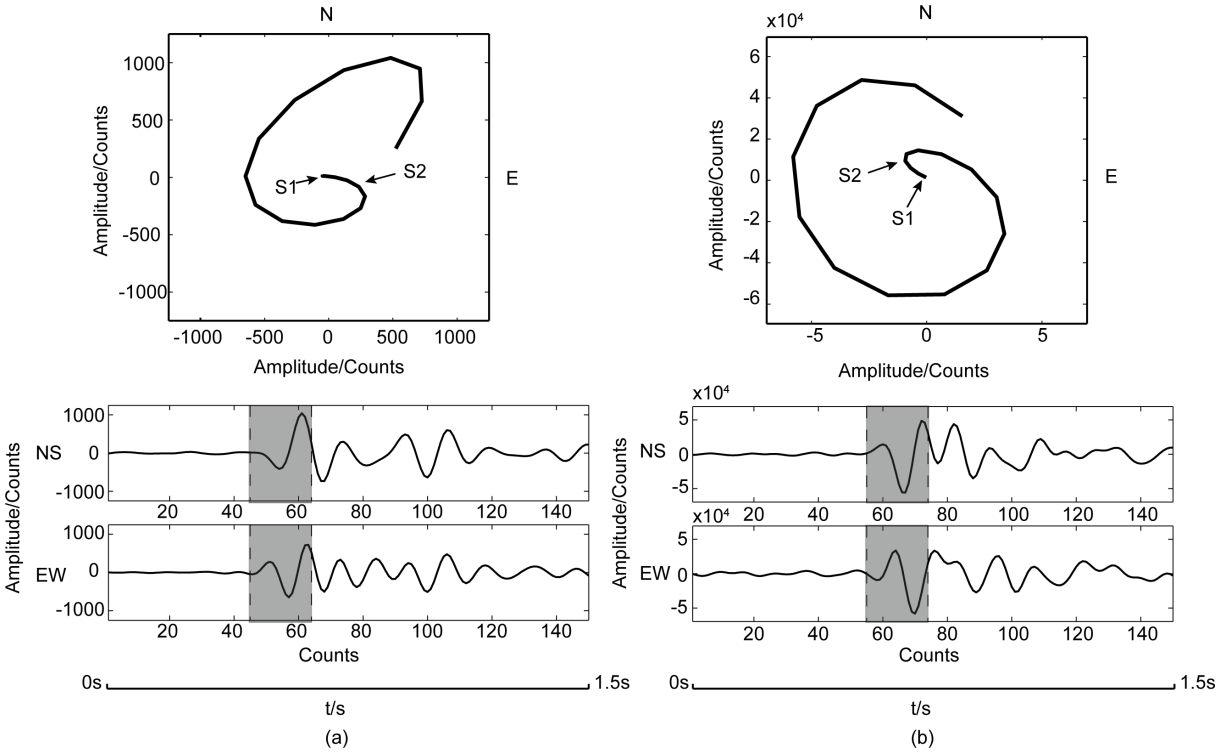

Figure 3. Polarization diagrams of the shear-wave splitting (SWS).

2005]. In this study, the shear-wave window is set to 45°. In addition, seismic waves from events within the shear-wave window are filtered in the frequency range of 1 to 10 Hz. Figures 2-4 demonstrate examples of the SWS analysis to obtain the splitting parameters.

As is shown in Figure 3, after the fast shear-wave arrival (S1) and before the slow shear-wave arrival (S2), the angle α between the direction of the particle trajectory of the shear-wave and due north is the polarization direction

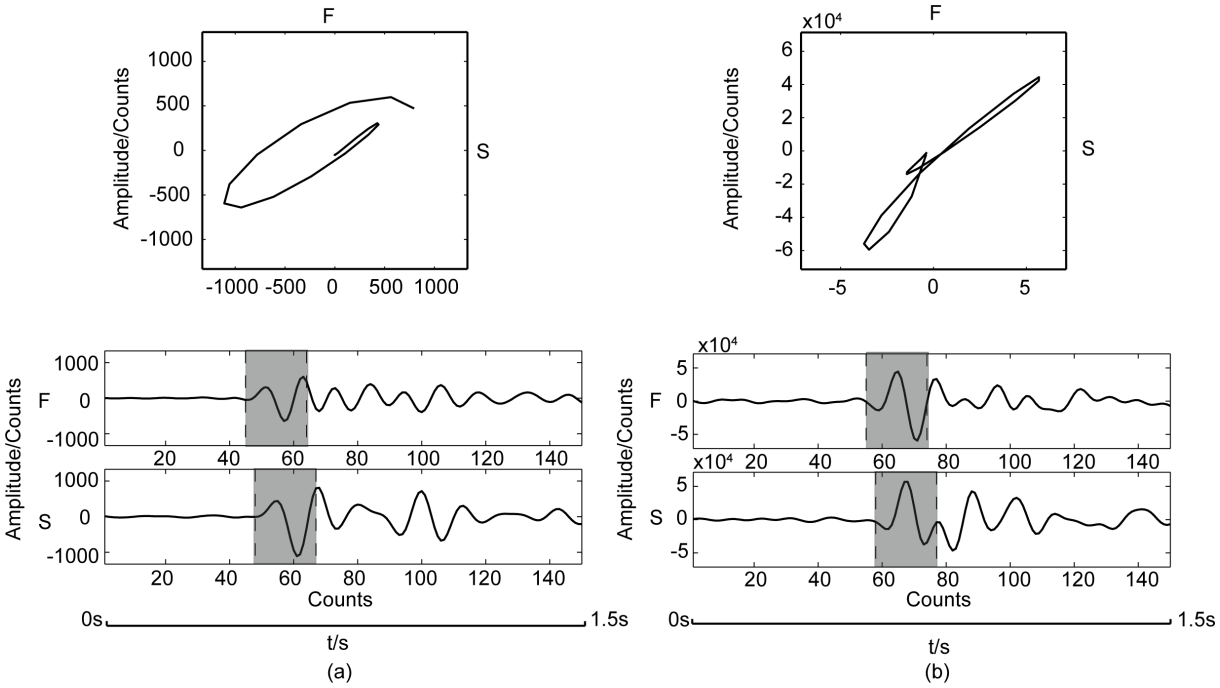

Figure 4. Polarization diagrams of fast and slow shear-wave after eliminating the effect of the time delays.

of the fast shear-wave, where $\alpha \in [0°, 180°]$. When the slow shear-wave arrives, it is superposed on the fast shear-wave, changing the motion trajectory of the shear-waves particle changes. As described above, the PFS of the seismic event recorded at Dxa06 and Dxt22 is 100° and 120°, respectively.

The fast and slow shear-waves can be separated by rotating the two horizontal components α counterclockwise simultaneously. In theory, the fast and slow shear-waves originate from the same source, and the time delay can be eliminated by advancing the time quantum of the slow shear-wave. After deducting the time delay, the particle trajectory becomes linear, therefore the SAM method can be self-verification [Gao et al., 2004]. The motion trajectories of the S-wave particle recorded at Dxa06 and Dxt22 have high linearity (Figure 4), proving the reliability of the SWS measurements for seismic events. Both the time delays at Dxa06 and Dxt22 are 0.03s.

4. Results

A total of 875 effective records at 50 temporary seismic stations were eventually determined applying the SAM method to analyze the seismic waveform data, and there were 36 stations with more than 3 effective measurements (Table 1). The lower hemispherical equal-area project rose diagram of the PFS in the study area was derived from the resulting SWS measurements (Figure 5). The mean direction of the PFS is $162° \pm 44°$, which is consistent with the regional maximum principal compressive stress direction [Cui et al., 2006; Qian et al., 2011]. The dominant PFS directions are in NW or NNW at most stations in the study area (Figure 6), i.e., stations Dxa02, Dxb01 and Dxb02. Due to the impact of the local complex geologic structure, a few stations exhibit two dominant directions, such as Dxy02, Dxy04 and Dxy16. In addition, some stations only have one or two effective records since there are few earthquakes near the stations, such as Dxc01, Dxt02, Dxt03 and Dxt06.

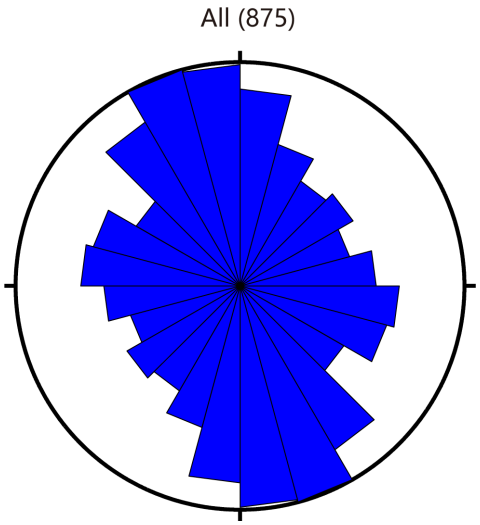

Figure 5. Lower hemispherical equal-area project rose diagram of fast shear-wave polarization in the study area.

4.1 Polarization directions of fast shear-wave

The lower hemispherical equal-area project rose diagram of the PFS displays a scattered pattern in the study area (Figure 5), but the dominant PFS direction is in NNW, consistent with the results in the same area obtained by Shi et al. [2012] and Tai et al. [2015], indicating the complexity of tectonic setting and stress field. Based on the spatial distribution of the PFS per station and the regional tectonic structure, the study area could be divided into two zones bounded about by 26°15′N, the zone N and the zone S. The PFS is different in the zone N and the zone S. Table 2 lists the SWS parameters in the two zones.

Codes of stations	No. of effective events	PFS ± Errors/(°)	Normalized TD ± Errors/(ms/km)
Dxa02	100	150.6 ± 30.8	5.23 ± 2.50
Dxa06	75	84.5 ± 19.9	4.48 ± 2.24
	54	2.3 ± 33.1	4.71 ± 2.43
Dxb01	12	156.0 ± 26.6	5.13 ± 2.05
Dxb02	14	171.1 ± 21.7	4.10 ± 2.53
Dxb04	11	113.5 ± 34.5	5.16 ± 2.02
	2	22.5 ± 3.5	5.66 ± 0.05
Dxb05	32	171.1 ± 19.2	5.94 ± 2.39
	8	96.1 ± 13.0	5.36 ± 2.10
Dxb06	33	93.2 ± 14.9	5.73 ± 2.13
Dxc01	2	74.5 ± 21.9	3.49 ± 0.50
Dxj04	22	69.3 ± 22.1	6.18 ± 2.19
	4	179.3 ± 13.0	6.46 ± 2.17
Dxj05	19	28.2 ± 36.7	4.59 ± 2.15
Dxj07	17	135.2 ± 41.2	3.59 ± 2.46
Dxt02	1	170.0	5.59
Dxt03	1	100.0	4.39
Dxt06	1	140.0	1.02
Dxt07	1	10.0	5.98
Dxt09	1	70.0	5.59
Dxt11	1	10.0	4.37
Dxt13	3	113.3 ± 28.9	5.93 ± 0.80
Dxt15	7	1.3 ± 13.4	3.36 ± 0.76
Dxt16	23	169.4 ± 14.7	5.79 ± 2.37
Dxt17	5	12.8 ± 16.7	5.75 ± 1.35
Dxt18	16	168.9 ± 32.1	5.91 ± 1.47
Dxt19	1	10.0	5.15
Dxt21	3	9.7 ± 4.5	4.73 ± 3.13
	1	50.0	6.02
Dxt22	2	144.5 ± 36.1	4.67 ± 0.32
Dxt24	8	105.5 ± 21.5	5.45 ± 1.95
	4	10.8 ± 14.3	4.01 ± 2.28
Dxt26	5	127.8 ± 35.4	4.89 ± 2.41
Dxt27	70	171.9 ± 27.8	5.74 ± 2.08
Dxt28	13	148.3 ± 11.6	5.83 ± 1.04
Dxt30	8	71.3 ± 15.3	5.51 ± 4.83
	3	170.0 ± 0.0	5.31 ± 2.80

Codes of stations	No. of effective events	PFS ± Errors/(°)	Normalized TD ± Errors/(ms/km)
Dxy01	10	6.5 ± 16.0	5.46 ± 1.97
	2	80.0 ± 42.4	6.32 ± 1.78
Dxy02	5	156.0 ± 8.9	5.51 ± 3.09
	1	35.0	3.19
Dxy04	11	95.8 ± 24.3	4.11 ± 1.89
	3	8.0 ± 7.2	3.98 ± 4.39
Dxy05	32	22.6 ± 31.7	4.53 ± 2.07
Dxy06	32	165.4 ± 32.6	5.13 ± 2.37
Dxy07	14	161.7 ± 19.4	4.90 ± 2.71
Dxy08	4	168.8 ± 31.2	3.88 ± 2.48
Dxy11	7	123.3 ± 19.2	5.08 ± 3.84
Dxy14	32	148.4 ± 43.9	3.23 ± 2.27
Dxy15	20	167.6 ± 25.5	5.43 ± 1.93
Dxy16	9	28.6 ± 18.6	5.50 ± 0.92
	5	143.0 ± 7.6	6.22 ± 0.94
Dxy17	24	151.8 ± 20.2	4.06 ± 2.00
	9	55.4 ± 22.8	4.62 ± 1.69
Dxy18	4	81.3 ± 6.3	4.26 ± 2.38
	1	150.0	5.90
Dxy19	2	172.0 ± 2.8	3.11 ± 0.84
Dxy20	1	120.0	6.81
Dxy21	2	95.0 ± 7.1	6.25 ± 3.28
Dxy22	55	167.1 ± 29.4	4.76 ± 2.10
Dxy23	4	35.0 ± 10.8	5.61 ± 1.40
Dxy24	2	179.0 ± 21.2	4.72 ± 0.02
Dxy25	1	160.0	2.96

Table 1. SWS parameters at stations in the study area.

Zones	No. of effective events	PFS ± Errors/(°)	Normalized TD ± Errors/(ms/km)
zone N	790	153.5 ± 45.0	5.02 ± 2.39
zone S	85	173.2 ± 30.1	5.51 ± 2.52

Table 2. The SWS parameters in the two zones.

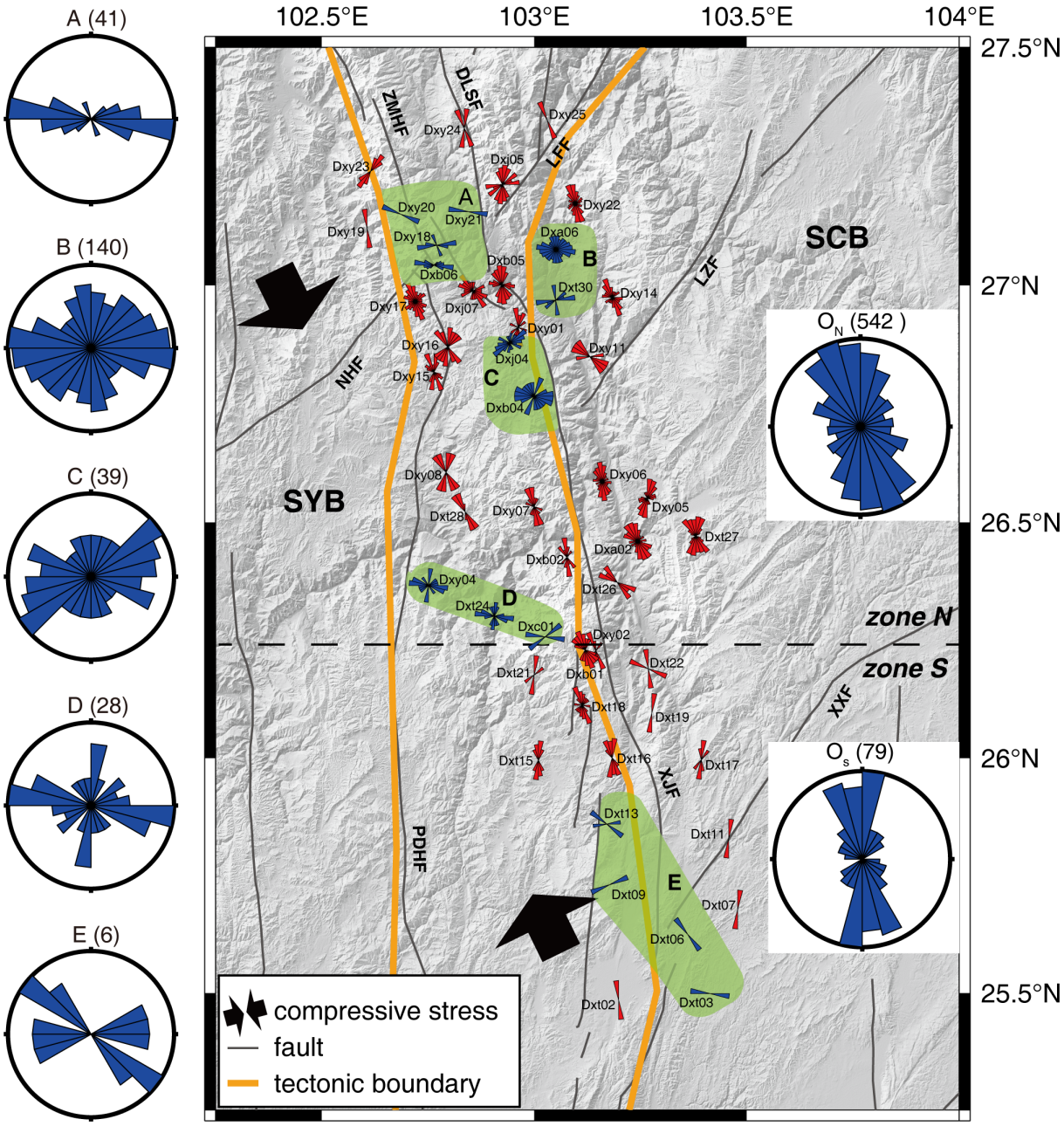

Figure 6. Lower hemispherical equal-area project rose diagrams of the polarizations of fast shear-wave (PFS). The rose diagrams at each station are shown in blue or in red. The green shaded areas outline the subzones A, B, C, D and E. The blue circled equal-area project rose diagrams depict SWS data in subzones.

A total of 790 effective measurements were acquired at 34 stations in the zone N, showing the significant variations in different zones. The zone N includes subzones A, B, C, D, which have considerably different PFS directions, and the larger subzone O_N excluding these four subzones, in which the dominant PFS is of better consistency (Table 3). Stations Dxb06, Dxy18, Dxy20, and Dxy21 are located in subzone A, where several faults converge to form the most complex fracture structure. Station Dxb06 shows consistent measurements, with the dominant PFS in nearly EW direction. Station Dxy18 has two dominant orientations in nearly EW and NNW, respectively. The effective records at stations Dxy20 and Dxy21 are less than 3, and the fast polarizations are WNW and nearly EW, respectively. Subzone B includes two stations, Dxa06 and Dxt30, to the east of the XJF and DLSF. Station Dxa06 has two dominant directions, and the dominant PFSs are in nearly EW and NS. The PFSs at station Dxt30 also display two apparently dominant directions in NEE and WNW, respectively. Subzone C is located on the west of the XJF, including stations Dxj04 and Dxb04. These two stations also have two dominant PFS directions,

with the main and secondary orientations in NEE and NS at station Dxj04, and in WNW and NNE at station Dxb04, respectively. The PFS pattern in subzone C is complicated, but still shows the dominant NNE direction. Subzone D includes stations Dxy04, Dxt24, and Dxc01, with the XJF to its east and the PDHF to its west. The dominant PFSs at Dxy04 and Dxt24 have good consistency, with nearly EW and NS, respectively. Station Dxc01 has only two effective records, with the dominant PFS in NEE direction. Subzone O_N has 23 stations that do not belong to subzones A, B, C, and D. Stations Dxa02, Dxt26, Dxt27, Dxy05, and Dxy06 are located on the east of the XJF, and the dominant PFS directions are in NW or NNW, except for NNE direction at station Dxy05. Stations Dxb02, Dxt28, Dxy07, and Dxy08 are situated between the XJF and PDHF, with the consistently dominant PFS in NNW. Stations Dxy11, Dxy14, and Dxy22 are located on both sides of the LZF, the dominant PFS directions are NW at Dxy11, NNW at Dxy14 and Dxy22. Station Dxj05, located between LFF and DLSF, shows a discrete PFS pattern, with a dominant PFS in NNE, parallel to the strike of LFF. Station Dxy23 is located on the west of the ZMHF and shows highly consistent measurements, with the dominant PFS in NE. Stations Dxb05, Dxj07, Dxy01, Dxy15-17 are located on the intersection area of several faults (i.e., XJF, PDHF, DLSF, LFF). The PFSs at these stations exhibit the complicated pattern, and the majority show two dominant directions. Station Dxb05 is located on the north end of the XJF, with two dominant PFS in nearly NS and EW directions, respectively. Station Dxj07 is situated on the ZMHF, and the dominant PFS direction is NE, consistent with the strike of the fault. Station Dxy01 displays two dominant orientations in nearly NS and EW. Station Dxy16 is located on the PDHF which is arc-shaped from the north to the south of the station. The PFS pattern shows two dominant directions, the main dominant direction is in NNE, consistent with the south of the arc-shaped fault, and the secondary dominant direction is NW, subparallel to the north of the arc-shaped fault. Station Dxy15 is located on the west of the PDHF, with the dominant polarization in NNW. Station Dxy17, located on the south of the intersection of the PDHF and Ninghui fault (NHF), has complex PFS pattern, and shows two dominant orientations in NNW and NE.

Subzones	No. of effective events	PFS ± Errors/(°)	Normalized TD ± Errors/(ms/km)
A	41	94.1 ± 17.1	5.62 ± 2.14
B	101	81.1 ± 26.8	4.42 ± 2.28
	39	179.0 ± 18.1	4.82 ± 2.38
C	39	62.9 ± 40.1	6.31 ± 2.37
D	19	92.5 ± 18.5	4.83 ± 2.12
	9	179.9 ± 22.1	3.50 ± 3.12
E	6	108.3 ± 29.3	4.80 ± 2.01
O_N	542	164.0 ± 35.4	5.05 ± 2.38
O_S	79	173.4 ± 26.2	5.44 ± 2.32

Table 3. The SWS parameters in subzones in the study area.

The 85 effective measurements were derived from 16 stations in the zone S. The zone S includes subzone E that consist of stations Dxt03, Dxt06, Dxt09, and Dxt13, and O_S excluding subzone E. Limited by weak seismicity in the zone S, most stations have less than three effective records. The dominant PFS in subzone E is in NWW. Only station Dxt13 has three effective records, whereas the others in subzone E have one effective record, with different dominant directions at each station. In subzone O_S, the dominant PFS is nearly NS. The PFS orientations at most stations have good consistency, parallel to the strike of the XJF. Station Dxt21 shows two dominant directions, with the main dominant orientation nearly in NS and the secondary one in NE (only one effective record).

4.2 Time delays of slow shear-wave

The TDS reveals the degree of seismic anisotropy [Crampin and Peacock, 2005; Gao et al., 2012], and is partly dependent upon the spatial distribution of the seismic sources relative to the receiver [Kapetanidis et al., 2021]. The studies have shown that the TDS is generally less than 0.3s [Crampin, 1984], while that at the stations located on complex structure area may be higher [Savage, et al., 1990]. Since the time delay reflects the overall effect along the ray path from the source to the station, a normalized time delay is proposed, i.e., the time delay per unit length of the ray path (ms/km). In this study, the normalized TDS varies from 2.96 to 6.81ms/km (Table 1), with the mean TDS of 4.96 ± 2.38 ms/km, which is identical to the results by Liang et al. [2020]. The TDS in the zone S is slightly higher than that in the zone N (Table 2). Tables 3 shows the TDS in subzones, with the largest in subzone C and the smallest in subzone D. Subzones A, B, and C are situated in the intersection area of several active faults, and the TDS in them is higher than that in other subzones. The resulting TDS suggest that the strength distribution of the seismic anisotropy in the study area exhibits obvious inhomogeneity, and the seismic anisotropy is stronger in the tectonically complex areas.

5. Discussions

The crustal anisotropy is mainly attributable to the presence of a large amount of stress-aligned fluid-saturated EDA (Extensive-Dilatancy Anisotropy) microcracks in the crustal rocks [Crampin and Peacock, 2005]. Observational studies have shown that the seismic anisotropy in the upper crust is possibly originated from two kinds of mechanisms [Gao et al., 2011]. One is the stress-induced anisotropy, that is, under the impact of the principal compressive stress, the microcracks perpendicular to the principal compressive stress in the crust tend to close, and the ones parallel to the principal compressive stress gradually open, making the PFS caused by microcracks parallel to the direction of the principal compressive stress [Crampin and Peacock, 2005]. The other one is structure-induced anisotropy, mainly due to alignments along active fault zones, sedimentary bedding planes, and aligned terrane minerals [Boness and Zoback, 2006; Shi et al., 2006; Gao et al., 2011]. The PFS derived from local earthquakes is controlled mostly by the regional stress field, which is parallel to the direction of *in situ* principal compressive stress and the dominant alignment direction of the EDA microcracks, but also is closely related to the fracture distribution, surface topography, and local structure [Gao et al., 1995, 2018; Shi et al., 2006, 2020]. In this study, using seismic data obtained from the dense QJ Array, a more detailed spatial pattern in the upper crustal anisotropy were acquired in the study area. The rose diagram of PFS at each station, characterized by heterogeneous distribution, implies the complexity of the regional compressive stress and the tectonic environment.

In the zone S, it is distributed several faults, PDHF striking NS, XJF striking NS, and Xundian-Xuanwei fault (XXF) striking NE. The dominant PFS directions are nearly in NS at most stations, i.e., subzone O_S, consistent with the strike of XJF (Figure 6 and Figure 7). Despite only limited effective records (only six) in subzone E, the dominant direction is in WNW, clearly different from the dominant NS direction in the zone S. It suggests that the upper crustal anisotropy in the zone S is controlled by XJF, nevertheless the local structure (i.e., the structural intersection area or the end of fault) causes the disparity in local crust deformation.

In the zone N, as the intersection area of different active faults, the PFS is complicatedly distributed (Figure 7). The stations in subzone O_N are located on both sides of XJF. The most dominant PFS directions are NNW, parallel to the regional principal compressive stress in WNW. The rose diagrams of the PFS in smaller local areas (i.e., subzones A, B, C and D) show more detailed information about the spatial pattern (Figure 6). In subzone A, the stations are close to the fault, and the dominant PFS direction is in WNW nearly EW, inconsistent with the strike of fault, but seemly parallel to the regional maximum principal compressive strain (Figure 6 and Figure 7). The resulting PFS in subzone A are quite different from those at surrounding stations, may imply the local distribution characteristics of *in situ* principal compressive stress. The two stations in subzone B have similar PFS patterns, with two dominant directions in nearly EW and NS, respectively. Though the PFS in subzone C is slightly scattered, it still shows the dominant direction in NNE. The subzones A, B, and C are adjacent and located in the intersection zone of several faults. This phenomenon reveals unique rock deformation in the upper crust, indicating that the direction of *in situ* principal compressive stress in these subzones differs from that of the regional principal compressive stress, consistent with the orientations of principal compressive strain in WNW on the west of the block boundary (Figure7). The stations in subzone D show obviously two dominant directions, nearly EW and NS, respectively.

The NS direction is highly consistent with the dominant PFS directions at most stations in the study area. The dual dominant PFS directions were reported once and interpreted as effects respectively from stress and faults or other tectonic structures [Gao et al., 2019]. Gao et al. [2020] presented that a mantle-scalar deep tectonic boundary striking EW possibly existed at 26°20′N. Considering that there are no faults striking nearly EW in subzone D and its adjacent zone, the dominant orientation nearly in EW may reveal the existence of crust-scalar tectonic line near 26°20′N (Figure 7). Liang et al. [2020] study seismic anisotropy in the north segment of the Xiaojiang fault zone and obtain two dominant directions in NNE and EW. By contrast, the dominant PFS nearly in EW acquired in this study is displayed in smaller local area, due to more effective measurements from more stations and longer seismic records. The SWS results obtained in the south segment of the Xiaojiang fault zone, near to 25°N, showed that the dominant direction is in NE, speculating that it is not controlled by the Xiaojiang fault, but affected by the SCB [Li et al., 2021]. The PFS in the zone N exhibited a discrete pattern, with the dominant NNW direction. In the observations elsewhere, the PFS could be jointly affected by stress and local structure in the tectonically complex area [Gao et al, 2018]. It is exactly demonstrated by SWS results in the zone N in this study. The direction of maximum principal compressive stress is spatially variable in the intersection area, the endpoint, or the bend position of the fault [Li, 1992; Gao et al.,

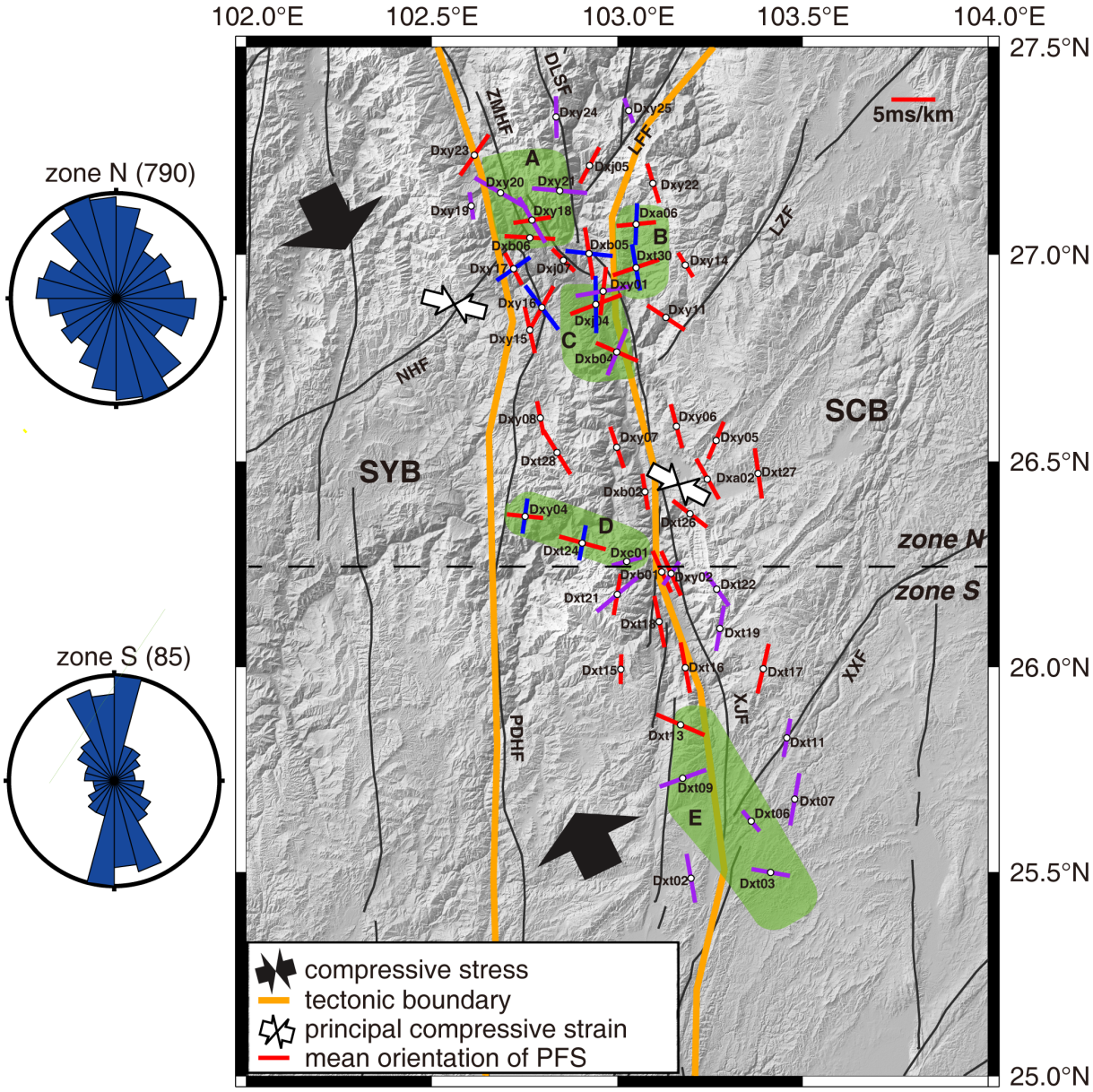

Figure 7. Spatial pattern of mean fast polarizations in the study area.The red and blue bars denote the main and secondary dominant orientations of the PFS, respectively, and the purple bars represent the effective SWS records less than 3.

1995], the heterogeneity in the crustal anisotropy may be derived from the residual characteristics of palaeo-stress [Aster and Shearer, 1992]. Based on the above analysis, it suggests that the anisotropic parameters in the subzones A, B, C, and D may reflect the spatial pattern of *in situ* principal compressive stress under the multiple influences of regional stress field and complex tectonic environment, and may be also related to the impact of the SCB.

The focal mechanism solutions of moderate earthquakes show that the tectonic stress field in the south of SYB is near- horizontal, and the direction of the principal compressional axis along the Xiaojiang fault from north to south is oriented from NW to NNW [Qian et al., 2011; Li et al., 2019]. Using data from the continuous dense GPS observations covering the north segment of the XJFZ, Fu et al. [2019] presented that the velocity field was in NE direction, the orientations of the principal compression axes changed from ~110° in the north subarea to ~130° in the south subarea. The PFS in the study area demonstrates a rotation tendency from north to south in the Xiaojiang fault zone and surrounding areas, from NNW to nearly NS.

6. Conclusions

Using seismic data from the temporary QJ Array deployed by the Institute of Geophysics, China Earthquake Administration, this study acquires the upper crustal anisotropy around the north segment of the Xiaojiang fault (XJF) zone by the shear-wave splitting (SWS) analysis. By analyzing the seismic waveform on local small earthquakes, a total of 875 effective SWS records were obtained at 50 stations. It presents a fine spatial pattern of the upper crustal anisotropy in the study area. The mean direction of the polarizations of fast shear-waves (PFS) is in $162° \pm 44°$ and the mean normalized time-delay is at 4.96 ± 2.38 ms/km. The PFS at each station displays obvious heterogeneity of the upper crustal anisotropy, indicating the complicated deep tectonic setting and the distorted stress field.

Based on the spatial distribution of the PFS per station and the regional geologic structure, the study area could be divided into two zones bounded about by 26°15′N, the zone N and the zone S. The dominant PFS direction in the zone S is in NNW. The dominant PFS direction in the zone N is also in NNW, although more scattered. However, the XJF are not a simple fault. The west XJF and the east XJF are almost parallel to each other, where some other faults intersect with the XJF in the study area. The seismic array is within a system of faults. Generally, the dominant PFS directions in two zones are parallel to the strikes of main faults. Most of stations show the dominant PFS directions consistent with maximum principal compressive stress.

Both in the zone N and in the zone S, there are a few smaller local subzones in which the PFS orientations are quite different from the surrounding areas. It probably displays the spatial pattern of *in situ* principal compressive stress. This phenomenon suggests the multiple influences of the regional stress field, the complex tectonic setting and maybe also the impact of the South China block (SCB).

However in the zones S and N, quite different dominant PFS orientations in smaller local subzones reveal the much more complex deformation in the upper crust in the intersection areas of faults. The important is that dominant PFS orientations in subzones show the detailed spatial pattern of *in situ* principal compressive stress and indicate the disparity in local crust deformation. It is also observed that there might be an upper-crustal scale tectonic line near 26°20′N (between 26°15′N and 26°25′N, see Figure 6). It seems in local area to coincide with the north-south boundary in the lithosphere anisotropy by Gao et al. [2020]. Nevertheless, due to the spatial distribution limitation of the temporary seismic array, it is still unclear about the extension of the upper-crustal scale of tectonic line.

Acknowledgements. We are grateful for data support from the field group of Qiaojia Seismic Array by Institute of Geophysics, China Earthquake Administration. This study is supported by National Natural Science Foundation of China Project (42074065). We also thank two reviewers for helpful comments.

References

Aster, R.C. and P. M. Shearer (1992). Initial shear wave particle motions and stres-s constraints at the Anza Seismic Network, Geophys. J. Int., 108, 740-748.

Bai, D., M. J. Unsworth, M. A. Meju, X. Ma, J. Teng, X. Kong, Y. Sun, L. Wang, C. Jiang, C. Zhao, P. Xiao and M. Liu (2010). Crustal deformation of the eastern Tibetan plateau revealed by magnetotelluric imaging, Nature Geosci., 3, 5, 358-262, doi: 10.1038/ngeo830.

Boness, N. L. and M. D. Zoback (2006). Mapping stress and structurally controlled crustal shear velocity anisotropy in California, Geology, 34,10, 825-828, doi:10.1130/g22309.1.

Cao, L., H. Kao, K. Wang, C. Chen, J. Mori, S. Ohmi and Y. Gao (2019). Spatiotemporal variation of crustal anisotropy in the source area of the 2004 Niigata, Japan earthquake, Bull. Seismol. Soc. Am., 109, 4, 1331-1342, doi: 10.1785/0120180195.

Crampin, S. (1978). Seismic-wave propagation through a cracked solid: Polarization as a possible dilatancy diagnostic, Geophys. J. Int., 53, 3, 467-496.

Crampin, S., E. M. Chesnokov and R. G. Hipkin (1984). Seismic anisotropy-the state of the art: II, Geophys. J. Int., 76, 1, 1-16.

Crampin, S., S. Chastin and Y. Gao (2003). Shear-wave splitting in a critical crust: III-preliminary report of multi variable measurements in active tectonics, J. Appl. Geophys., 54, 265-277.

Crampin, S. and S. Peacock (2005). A review of shear-wave splitting in the compliant crack-critical anisotropic Earth, Wave Motion, 41, 1, 59-77.

Crampin, S., Y. Gao and S. Peacock (2008). Stress-forecasting (not predicting) earthquakes: a paradigm shift?, Geology, 26, 5, 427-430, doi:10.1130/g24643a.1.

Crampin, S. and Y. Gao (2018). Evidence supporting New Geophysics, Earth Planet. Phys., 2, 3, 3-18, doi: 10.26464/epp2018018.

Clark, M. K. and L. H. Royden (2000). Topographic ooze: Building the eastern margin of Tibet by lower crustal flow, Geology, 28, 8, 703-706.

Cui, X., F. Xie and H. Zhang (2006). Recent tectonic stress field zoning in Sichuan-Yunnan region and its dynamic interest, Acta Seismologica Sinica (English edition), 19, 5, 485-496.

Fu, Z., L. Xu and Y. Wang (2019). Seismic Risk on the Northern Xiaojiang Fault Implied by the Latest and Nearest GPS Observations, Pure Appl. Geophys., 177(2), 661-679, doi: 10.1007/s00024-019-02347-5.

Gao, Y., S. Zheng and Y. Sun (1995). Crack-induced anisotropy in the crust from shear wave splitting observed in Tangshan region, North China, Acta Seismologica Sinica (English edition), 8, 3, 351-263.

Gao, Y., P. Wang, S. Zheng, M. Wang, Y. Chen and H. Zhou (1998). Temporal changes in shear-wave splitting at an isolated swarm of small earthquakes in 1992 near Dongfang, Hainan Island, southern China, Geophys. J. Int., 135, 1, 102-112, doi: 10.1046/j.1265-246X.1998.00606.x

Gao, Y. and S. Crampin (2004). Observations of stress relaxation before earthquakes, Geophys. J. Int., 157, 2, 578-582, doi: 10.1111/j.1265-246X.2004.02207.x.

Gao, Y., X. Liu, W. Liang and P. Hao (2004). Systematic analysis method of shear-wave splitting: SAM software system, Earthq. Res. China (English edition), 18, 4, 265-372.

Gao, Y. and S. Crampin (2006). A further stress-forecast earthquake (with hindsight), where migration of source earthquakes causes anomalies in shear-wave polarizations, Tectonophysics, 426, 3-4, 253-262.

Gao, Y., J. Wu, Y. Fukao, Y. Shi and A. Zhu (2011). Shear-wave splitting in the crust in North China: stress, faults and tectonic implications, Geophys. J. Int., 187, 642-654.

Gao, Y., J. Wu and L. Tai (2012). Shear-wave splitting in the crust: regional compressive stress from polarizations of fast shear-waves, Earthquake Science, 25, 1, 35-45.

Gao, Y., Y. Shi and A. Chen (2018). Crustal seismic anisotropy and compressive stress in the eastern margin of the Tibetan Plateau and the influence of the M_S8.0 Wenchuan earthquake, Chinese Science Bull. (in Chinese with extended English abstract and caption), 63, 19, 1934-1948, doi: 10.1260/N972018-00317.

Gao, Y., A. Chen, Y. Shi, Z. Zhang and L. Liu (2019). Preliminary analysis of crustal shear-wave splitting in Sanjiang lateral collision zone of the SE margin of the Tibetan Plateau and its tectonic implications, Geophys. Prospect., 67, 9, 2432-2449, doi:10.1111/1265-2478.12870.

Gao, Y., Y. Shi and Q. Wang (2020). Seismic anisotropy in the southeastern margin of the Tibetan Plateau and its deep tectonic significances, Chinese J. Geophys. (in Chinese with English abstract and captions), 63, 3, 802-816, doi: 10.6038/cjg2020O0033.

Huang, Z., L. Wang, M. Xu and D. Zhao (2018). P-wave anisotropic tomography of the SE Tibetan Plateau: Evidence for the crustal and upper-mantle deformations, J. Geophys. Research: Solid Earth, 123(10), 8957-8978, doi: 10.1029/2018jb016048.

Jiang, E., K. H. Liu, Y. Gao, X. Fu and S. S. Gao (2021). Spatial variations of upper crustal anisotropy along the San Jacinto Fault Zone in Southern California: Constraints from shear wave splitting analysis, J. Geophys. Res.: Solid Earth, 126, e2020JB020876, doi: 10.1029/2020jb020876.

Kapetanidis, V., G. Michas, G. Kaviris and F. Vallianatos (2021). Spatiotemporal properties of seismicity and variations of shear-wave splitting parameters in the Western Gulf of Corinth (Greece), Applied Sci., 11, 14, 6573. https://doi.org/10.3390/app11146573.

Kaviris, G., P. Papadimitriou, P. Kravvariti, V. Kapetanidis, A. Karakonstantis, N. Voulgaris and K. Makropoulos (2015). A detailed seismic anisotropy study during the 2011-2012 unrest period in the Santorini Volcanic Complex, Phys. Earth Planet. Inter., 238, 51-88.

Kaviris, G., I. Spingos, C. Millas, V. Kapetanidis, I. Fountoulakis, P. Papadimitriou, N. Voulgaris and G. Drakatos (2018). Effects of the January 2018 seismic sequence on shear-wave splitting in the upper crust of Marathon (NE Attica, Greece), Phys. Earth Planet. Inter., 285, 45-58.

Kreemer, C., G. Blewitt and E. C. Klein (2014). A geodetic plate motion and Global Strain Rate Model, Geochem., Geophys., Geosyst., 15, 10, 3849-3889, doi: 10.1002/2014gc005407.

Kong, F., J. Wu, K. H. Liu and S. S. Gao (2016). Crustal anisotropy and ductile flow beneath the eastern Tibetan Plateau and adjacent areas, Earth Planet. Sci. Lett., 442, 72-79, doi: 10.1016/j.epsl.2016.03.003.

Li, J., Q. Wang, Z. Cui, P. Zhang, L. Zhou and H. Zhou (2019). Characteristics of focal mechanisms and stress field in the eastern boundary of Sichuan-Yunnnan block and its adjacent area, Seismol. Geol. (in Chinese with English abstract), 41(6), 1395-1412.

Li, L., Q. Chen, F. Niu, J. He and H. Fu (2013). Estimates of deep slip rate along the Xiaojiang fault with repeating microearthquake data, Chinese J. Geophys. (in Chinese with English abstract and captions), 56, 10, 3373-3384, doi: 10.6038/cjg20131013.

Li, Q. (1992). A study on current stress field and seismic danger areas in the central-western Yunnan province, Northwestern Seismological Journal (in Chinese with English abstract), 14, 2, 72-78.

Li, X., D. Bai, X. Ma, Y. Chen, I. M. Varentsov, G. Xue, S. Xue and I. Lozovsky (2019). Electrical resistivity structure of the Xiaojiang strike-slip fault system (SW China) and its tectonic implications, Journal of Asian Earth Sciences, 176, 57-67, doi: 10.1016/j.jseaes.2019.01.031.

Li, Y., Y. Gao, Y. Shi and P. Wu (2021). Preliminary seismic anisotropy in the upper crust of the south segment of Xiaojiang faults and its tectonic implications, Earthquake Science, 34, 1, 64-76, doi: 10.29382/eqs-2020-0059.

Liang, H., Z. Fu, C. Li and L. Xu (2020). Preliminary analysis of the shear-wave splitting observations from the Qiaojia seismic array, Earthquake Sci., 33, 2, 82-97, doi: 10.29382/eqs-2020-0082-04.

Liang, S., W. Gan, C. Shen, G. Xiao, J. Liu, W. Chen, X. Ding and D. Zhou (2013). Three-dimensional velocity field of present-day crustal motion of the Tibetan Plateau derived from GPS measurements, J. Geophys. Res.: Solid Earth, 118, 5722-5732, doi: 10.1002/2013jb010503.

Long, M. D. and P. G. Silver (2008). The subduction zone flow field from seismic anisotropy: a global view, Science, 319, 5861, 315-318, doi: 10.1126/science.1150809.

Qian, X., J. Qin and L. Liu (2011). Study on recent tectonic stress field in Yunnan region, Seimology and Geology (in Chinese with English abstract), 33, 1, 91-106.

Royden, L. H., B. C. Burchfiel, R. W. King, E. Wang, Z. Chen, F. Shen and Y. Liu (1997). Surface deformation and lower crustal flow in eastern Tibet, Science, 276, 5313, 788-790, doi:10.1126/science.276.5313.788.

Savage, M. K., W. A. Peppin and U. R. Vetter (1990). Shear wave anisotropy and stress direction in and near Long Valley Caldera, California, 1979-1988, J. Geophys. Res., 95, B7, 11165-11177.

Savage, M. K. (1998). Lower crustal anisotropy or dipping boundaries? Effects on receiver functions and a case study in New Zealand, J. Geophys. Res., 103, B7, 15069-15087, doi: 10.1029/98jb00795.

Sherrington, H. F., G. Zandt and A. Frederiksen (2004). Crustal fabric in the Tibetan Plateau based on waveform inversions for seismic anisotropy parameters, J. Geophys. Res., 109, JB02312, doi:10.1029/2002JB002345.

Shen, Z., J. Lü, M. Wang and R. Bürgmann (2005). Contemporary crustal deformation around the southeast borderland of the Tibetan Plateau, J. Geophys. Res., 110, B11409, doi: 10.1029/2004jb003421.

Shi, Y., Y. Gao, J. Wu, Y. Luo and Y. Su (2006). Seismic anisotropy of the crust in Yunnan, China: polarizations of fast shear-wave, Acta Seismologica Sinica (English edition), 19, 6, 620-632.

Shi, Y., Y. Gao, Y. Su and Q. Wang (2012). Shear-wave splitting beneath Yunnan area of southwest China, Earthquake Sci., 25, 1, 25-34.

Shi, Y., Y. Gao, X. Shen and K. H. Liu (2020). Multiscale spatial distribution of crustal seismic anisotropy beneath the northeastern margin of the Tibetan plateau and tectonic implications of the Haiyuan fault, Tectonophysics, 774, 228274, doi: 10.1016/j.tecto.2019.228274.

Tai, L., Y. Gao, G. Liu and Z. Xiao (2015). Crustal seismic anisotropy in the southeastern margin of Tibetan Plateau by ChinArray data: shear-wave splitting from temporary observations of the first phase, Chinese J. Geophys. (in Chinese with English abstract and captions), 58, 11, 4079-4091.

Silver, P. and L. Flesch (2007). Seismic anisotropy of upper mantle in eastern Tibetan Plateau and related crust-mantle coupling pattern, Science in China Series D-Earth Sciences (English edition), (08), 1150-1160.

Wang, E, B. C. Burchfiel, L. H. Royden, L. Chen, J. Chen, W. Li and Z. Chen (1998). Late Cenozoic Xianshuihe-Xiaojiang, Red River, and Dali fault systems of southwestern Sichuan and central Yunnan, China, Special Paper of the Geological Society of America, 327, 1-108, doi:10.1130/0-8137-2327-2.1.

Wang, X., J. Lü, Z. Xie, F. Long, X. Zhao and Y. Zheng (2015). Focal mechanisms and tectonic stress field in the North-South Seismic Belt of China, Chinese J. Geophys. (in Chinese with English abstract and captions), 58, 11, 4149-4162, doi:10.6038/cjg20151122.

Wu, J., T. Yang, W. Wang, Y. Ming and Z. Zhang (2013). Three dimensional P-wave velocity structure around Xiaojiang fault system and its tectonic implications, Chinese J. Geophys. (in Chinese with English abstract and captions), 56, 7, 2257-2267, doi: 10.6038/cjg20130713.

Xu, T., M. Zang, X. Tian, Y. Zheng, Z. Bai, C. Wu, Z. Zhong and J. Teng (2014). Upper crustal velocity of Lijiang-Qingzhen profile and its relationship with the seismogenic environment of the MS6.5 Ludian earthquake, Chinese Journal of Geophysics (in Chinese with English abstract and captions), 57, 9, 3069-3079, doi: 10. 6038/cjg20140932.

Xu, X., X. Wen, R. Zheng, W. Ma, F. Song and G. Yu (2003). Pattern of latest tectonic motion and its dynamics for active blocks in Sichuan-Yunnan region, Science in China Series D-Earth Sciences (English edition), 46, 210-226.

Yang, B., Y. Liu, H. Dahm, K. H. Liu and S. S. Gao (2017). Seismic azimuthal anisotropy beneath the eastern United States and its geodynamic implications, Geophys. Res. Lett., 44, 6, 2670-2678, doi: 10.1002/2016gl071227.

Yin, A. and T. M. Harrison (2000). Geologic evolution of the Himalayan-Tibetan orogen, Annual Review of Earth and Planetary Sciences, 28, 211-280.

Zhang, B., S. Zhang, T. Wu and Y. Hua (2018). Upper crustal anisotropy from local shear-wave splitting and crust-mantle coupling of Yunnan, SE margin of Tibetan Plateau, Geod. Geodyn. (English edition), 9, 04, 302-311.

Zhang, Y. and Y. Gao (2017). The characteristics of crustal shear-wave splitting in North-South seismic zone revealed by near field recordings of two observation periods of ChinArray, Chinese Journal of Geophysics (in Chinese with English abstract and captions), 60, 6, 2181-2199, doi: 10.6038/ cjg20170613.

Zhang, Z., Y. Deng, J. Teng, C. Wang, R. Gao, Y. Chen and W. Fan (2011). An overview of the crustal structure of the Tibetan plateau after 35 years of deep seismic soundings, J. Asian Earth Sci., 40, 4, 977-989, doi: 10.1016/j.jseaes.2010.03.010.

Zhao, Y., L. Guo, Z. Guo, Y. J. Chen, L. Shi and Y. Li (2020). High resolution crustal model of SE Tibet from joint inversion of seismic P-wave travel-times and Bouguer gravity anomalies and its implication for the crustal channel flow, Tectonophysics, 792, 228580, doi: 10.1016/j.tecto.2020.228580.

Zheng, C., Z. Ding and X. Song (2016). Joint inversion of surface wave dispersion and receiver functions for crustal and uppermost mantle structure in Southeast Tibetan Plateau, Chinese J. Geophys. (in Chinese with English abstract and captions), 59, 9, 3223-3236, doi: 10.6038/ cjg20160908.

Zheng, G., H. Wang, T. J. Wright, Y. Lou, R. Zhang, W. Zhang, C. Shi, J. Huang and N. Wei (2017). Crustal Deformation in the India-Eurasia Collision Zone From 25 Years of GPS Measurements, J. Geophys. Res.: Solid Earth, 117, 13, B04403, doi:10.1002/2017JB014465.

Zheng, T., Z. Ding, J. Ning, L. Chang, X. Wang, F. Kong, K. H. Liu and S. S. Gao (2018). Crustal Azimuthal Anisotropy Beneath the Southeastern Tibetan Plateau and its Geodynamic Implications, J. Geophys. Res. Solid Earth, 123, doi: 10.1029/2018jb015995.

***CORRESPONDING AUTHOR: Yuan GAO**,
Key Laboratory of Earthquake Prediction, Institute of Earthquake Forecasting, China Earthquake Administration,
Beijing 100036, China
e-mail: qzgyseis@163.com